



Master Thesis

Assembly and proving of a wave front
sensing confocal Scanning Laser
Ophthalmoscope

Christina Schwarz

Supervisors: Prof. Dr. Frederick W. Fitzke, University College London (UK)
Prof. Dr. Josef F. Bille, Universität Heidelberg (Germany)

March 29, 2007

Abstract:

Confocal Scanning Laser Ophthalmoscopy is used to image the fundus of the living eye. In theory, this technique can be used to observe single cells of the retina. Unfortunately, vision of most eyes is decreased by higher-order aberrations, that cannot be corrected by glasses or contact lenses. This is also the reason why resolution in confocal Scanning Laser Ophthalmoscopy is not as high as expected. By the use of adaptive optics (AO) resolution can be dramatically increased. Implementing a wave front sensor into a conventional confocal Scanning Laser Ophthalmoscope (cSLO), therefore, is the first step to set up a compact adaptive-optical cSLO. In this work a Shack-Hartmann wave front sensor was implemented into a slightly modified Heidelberg Retina Tomograph (HRT) and aberrations of model eyes were measured. Results show that this system is now ready for testing on living eyes.

Zusammenfassung:

Um den Augenhintergrund des lebendigen Auges abzubilden bedient man sich der konfokalen Scanning Laser Ophthalmoskopie. Theoretisch kann diese Technik genutzt werden, um einzelne Zellen der Retina zu beobachten. In der Praxis ist das Sehvermögen des Auges jedoch im Allgemeinen durch Aberrationen höherer Ordnungen beeinträchtigt, die weder mit Brille noch mit Kontaktlinsen korrigiert werden können. Aus demselben Grund ist die Auflösung eines konfokalen Scanning Laser Ophthalmoskops (cSLO) in in-vivo-Anwendung am Auge schlechter als erwartet. Durch das Prinzip der adaptiven Optik (AO) kann die Auflösung erheblich verbessert werden. Der Einbau eines Wellenfrontsensors in ein handelsübliches cSLO ist daher der erste Schritt, um ein kompaktes adaptiv-optisches cSLO zu entwickeln. In dieser Arbeit wurde ein Hartmann-Shack-Wellenfrontsensor in einen leicht veränderten Heidelberg Retina Tomographen (HRT) eingebaut und Aberrationen von Modellaugen gemessen. Die Ergebnisse haben gezeigt, dass dieser Aufbau nun bereit ist, an lebenden Augen getestet zu werden.

Contents

1	Introduction	1
2	The Human Eye	3
2.1	Anatomy	3
2.2	Ametropia	5
2.2.1	Myopia	6
2.2.2	Hyperopia	6
2.2.3	Astigmatism	7
2.2.4	Irregular Astigmatism	8
2.3	Dynamics of the Eye	8
2.4	Pathology	9
2.4.1	Age-related Macular Degeneration	10
2.4.2	Glaucoma	11
3	Confocal Scanning Laser Ophthalmoscopy	12
3.1	Principle of the cSLO	12
3.2	Resolution of Confocal Images	14
3.3	The Heidelberg Retina Tomograph	15
4	Adaptive Optics	16
4.1	The Wave Front and Wave Aberrations	16
4.2	Wave Front Sensors	19
4.3	Phase Modulators	22
4.4	The Control Algorithm	23

5	Setup	27
5.1	Hardware	27
5.2	Software	31
6	Results	32
6.1	Measurement and Evaluation	32
6.2	Discussion and Future Prospect	36
	Bibliography	38

Chapter 1

Introduction

Adaptive correction has its origin in astronomy. Horace Babcock was the first one who proposed solution to the problem of imaging stars with ground-based telescopes [1], which lies in the turbulent, rapidly changing atmosphere that significantly degrades image quality. As the technique of measuring atmospheric aberrations and building and controlling deformable mirrors is very complex, it took several years until the first successful demonstration. Most of the ground-based telescopes around the world are now equipped with this technique and therefore can sometimes achieve images with even higher resolution than those obtained by the Hubble space telescope [2].

The use of AO is not limited to astronomical imaging, and in the past few decades there has been a rapid expansion in the applications for which adaptive optics has proven valuable. Vision scientists and ophthalmologists have long been interested in imaging cellular structures in the living retina to examine photoreceptor properties *in vivo*, and to more precisely characterize retinal disease. Unfortunately, nearly every human eye suffers from higher order aberrations induced mainly by the lens and cornea that degrade retinal image quality (like the turbulent atmosphere degrades image quality in astronomy) and limit spatial vision. So a promising application of AO is the imaging of the living retina at high resolution, which became possible in the meantime.

One of the pathfinders of adaptive optics in vision science was Smirnov who employed a subjective vernier task to measure the retinal misalignment of rays entering through different parts of the pupil. He recognized that this method could theoretically allow for the fabrication of contact lenses that corrected higher order aberrations in the eye but thought that the lengthy calculations required to compute the wave aberration made his approach impractical. He could not foresee the rapid development of computer technology that would eventually make it possible to do these calculations in a matter of milliseconds.

1. Introduction

The headstone for clinical adoption of adaptive optics in vision science was laid when Junzhong Liang demonstrated at the University of Heidelberg, that it was possible to adapt the Shack-Hartmann wave front sensor, typically used in optical metrology, to measure the eye's wave aberration [3]. This proved to be the key development that paved the way to closed-loop AO systems for the eye. The simplicity of the Shack-Hartmann method and the fact that it is the wave front sensor used in most astronomical AO systems made it easier to translate adaptive optics to the eye. This method was also amenable to automation and the wave aberration could be measured and corrected in real-time [4].

It was also at the University of Heidelberg the first attempt of using a deformable mirror to improve retinal images in a scanning laser ophthalmoscope was made. Thus they were able to correct the astigmatism in one subject's eye by use of a deformable mirror [5].

The application of AO to increase the resolution of retinal images promises to greatly extend the information that can be obtained from the living retina. Adaptive optics now allows the routine examination of single cells in the eye such as photoreceptors and leucocytes, providing a microscopic view of the retina that could previously only be obtained in excised tissue. The ability to see these structures *in vivo* provides the opportunity to noninvasively monitor normal retinal function, the progression of retinal disease, and the efficacy of therapies for disease at a microscopic spatial scale.

In this work a compact wave front sensing confocal Scanning Laser Ophthalmoscope is built out of a conventional Heidelberg Retina Tomograph and tested in order to set up an adaptive-optical confocal Scanning Laser Ophthalmoscope later on.

This work is organized as follows:

In chapter 2 the necessary medical background for this work is given, including ametropia, aberrations, and the major diseases of the eye. The technical background of confocal Scanning Laser Ophthalmoscopes is given in chapter 3. Theory for adaptive optics is explained in chapter 4, as well as all technical components of an adaptive-optical closed-loop system. In chapter 5 I will describe the setup for this work in detail. Finally, results are presented and discussed in chapter 6. Here also a future prospect is given.

Chapter 2

The Human Eye

This chapter will give a brief review on the anatomical structure and basic function of the eye [6, 7, 8]. As there are many diseases that deteriorate vision quality and for which retinal imaging is advantageous only two major diseases are presented here [9].

2.1 Anatomy

Although the eye is commonly referred to as the globe, it is not really a true sphere but a composition of two spheres with different radii, one set into the other as shown in Figure 2.1. The anterior sphere is the smaller and more curved of the two and is called the cornea, which is a completely transparent structure. The posterior sphere is a white opaque fibrous structure called the sclera. The cornea and the sclera encase the eye and form a protective shell for all the delicate tissues within. The human eye measures approximately 24 mm in all its main diameters in normal adults.

Most of the refraction of the eye takes place through the **cornea** having a convex surface, that acts as a powerful lens. Thereby, the refraction of the anterior side of the cornea is responsible for 49 dpt of the refraction¹ and the posterior side of the cornea again detracts 6 dpt from it². As the cornea has a thickness of less than 1 mm at its periphery the lens-maker's formula (which says that for a thin lens, the power is approximately the sum of the surface powers) can be used and in doing so this yields a refractive power of $D_{cornea} = 43$ dpt altogether [8].

The opaque **sclera** forms the posterior five sixths of the eye's protective coat. At its most posterior portion, the site of attachment of the optic nerve, the

$$\begin{aligned} {}^1D_{ant} &= \frac{(n_{cornea} - n_{air})}{r_{ant}} = \frac{(1.377 - 1)}{0.0077 \text{ m}} \approx 49 \text{ dpt} \\ {}^2D_{post} &= \frac{(n_{aq} - n_{cornea})}{r_{post}} = \frac{(1.336 - 1.377)}{0.0065 \text{ m}} \approx -6 \text{ dpt} \end{aligned}$$

2. The Human Eye

sclera becomes a thin, sieve like structure called the lamina cribrosa. It is through this sieve that the retinal fibers leave the eye to form the optic nerve. The pigmented **iris** is perforated at its center by a circular aperture called the **pupil** and therefore has the physical meaning of a pinhole. Contraction of the iris, which occurs in response to bright light, is accomplished by the activity of a flat, washer like muscle buried in its substance just surrounding the pupil opening. Between the iris and the cornea the anterior chamber of the eye is located that is filled by a clear fluid called the aqueous humor. The ciliary muscle within the **ciliary body** releases the tension of the zonular fibers, controlling the size and shape of the lens. This in turn allows the lens of the eye to bulge and increase its power. Therefore, this muscle directly controls the focusing ability of the eye, a process which is called accommodation.

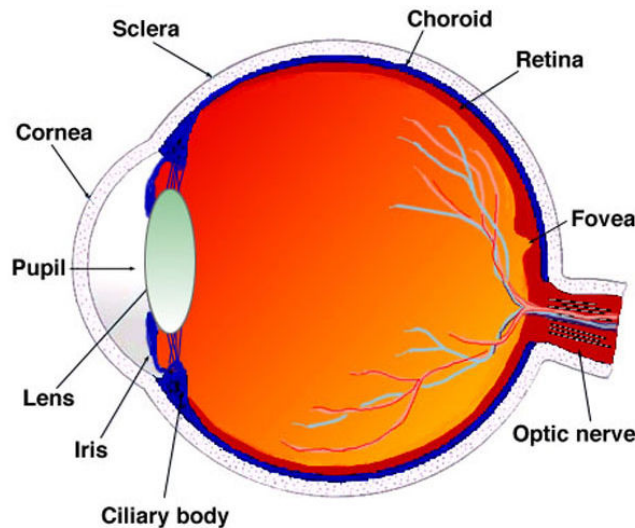


Figure 2.1: *This figure shows the sagittal section of the human eye [7].*

The **lens** of the eye is a transparent biconvex structure situated right behind the iris and therefore about 5 mm behind the cornea. The diameter of the lens is about 9 to 10 mm and its refractive power is about 19 dpt in the emmetropic eye. To calculate the refractive power of the eye in total Gullstrand's formula³ is used and equals approximately 59 dpt.

The **choroid's** main function is to provide nourishment for the outer layers of the retina. The **retina** varies in thickness and elevation, according to key anatomical features, pathological conditions, and changes with age. It contains all the sensory receptors for the transmission of light which are divided

³ $D = D_{cornea} + D_{lens} - \frac{d}{n_{aq}} D_{cornea} D_{lens} = 43 \text{ dpt} + 19 \text{ dpt} - \frac{0.005 \text{ m}}{1.336} \cdot 43 \cdot 19 \text{ dpt}^2 \approx 59 \text{ dpt}$

2. The Human Eye

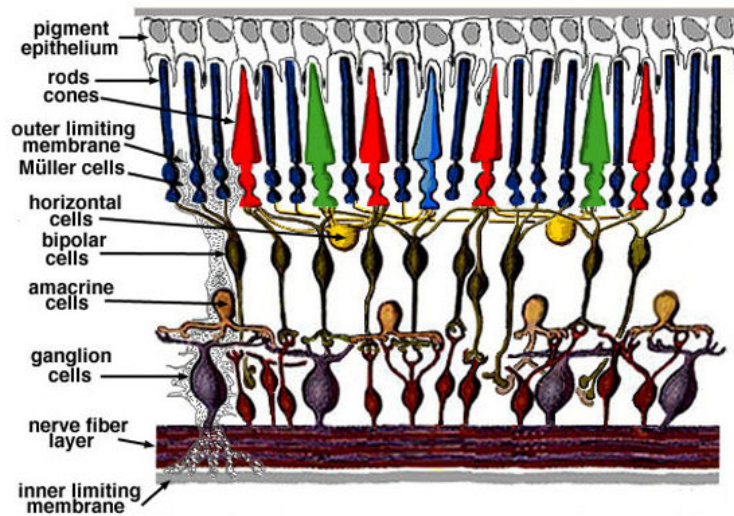


Figure 2.2: *This figure shows a simplistic scheme of a human retina [7].*

into two main populations - the rods (~ 125 million) and the three different types of cones (~ 6 million). Rods function best in dim light whereas the cones function best under daylight conditions. They enable us to see small visual details with great acuity. Vision with the rods is relatively poor but they detect movement. Color vision is totally dependent on the integrity of the cones which show different spectral sensitivities. According to their maximal spectral reflectivity at 565 nm, 535 nm, and 440 nm respectively, they are assigned to the fundamental colors red, green and blue. The cones form a concentrated area in the retina known as the fovea, which lies in the center of the macula lutea, usually less than 10° from the optical axis of the eye. Damage to this area can severely reduce the ability to see directly ahead. When we see an object the following process takes place: Light rays enter the eye through the cornea, move through the pupil, which is surrounded by Iris to keep out extra light, the crystalline lens and the vitreous humor and fall onto the retina, which processes and converts incident light to neuron signals. The neuron signals finally are transmitted through the optic nerve towards the brain, where the images are interpreted.

2.2 Ametropia

More than half of the world's population is affected by any kind of ametropia. Among the monochromatic aberrations the most frequently are defocus (myopia and hyperopia, respectively) and astigmatism. The amount of aberration

2. The Human Eye

tion for the complete eye arises from the amount of aberration of the cornea and the amount of aberrations of the internal optics and was found to be smaller than the sum of the last-mentioned. Indeed this fact indicates that the first surface of the cornea and internal optics partially compensate for each others aberrations and produce an improved retinal image [10] but in general it is still far from perfect. Nowadays these aberrations can be corrected in most instances by spectacles or contact lenses.

2.2.1 Myopia

Myopia or nearsightedness is a refractive defect of the eye in which collimated light produces image focus in front of the retina when accommodation is relaxed. This occurs from the eye being too long for its optical power or optically too powerful for its axial length. People with myopia typically can see nearby objects clearly but distant objects appear blurred. Myopia can be corrected by a concave lens placed in front of the eye.

2.2.2 Hyperopia

Hyperopia, also known as hypermetropia or colloquially as farsightedness, is a defect of vision caused by the eyeball being too short or the lens not being able to become round enough. People affected by hyperopia are unable to focus on near objects, and in extreme cases unable to focus on objects at any distance. As an object moves towards the eye, the eye must increase its power to keep the image on the retina. If the power of the cornea and

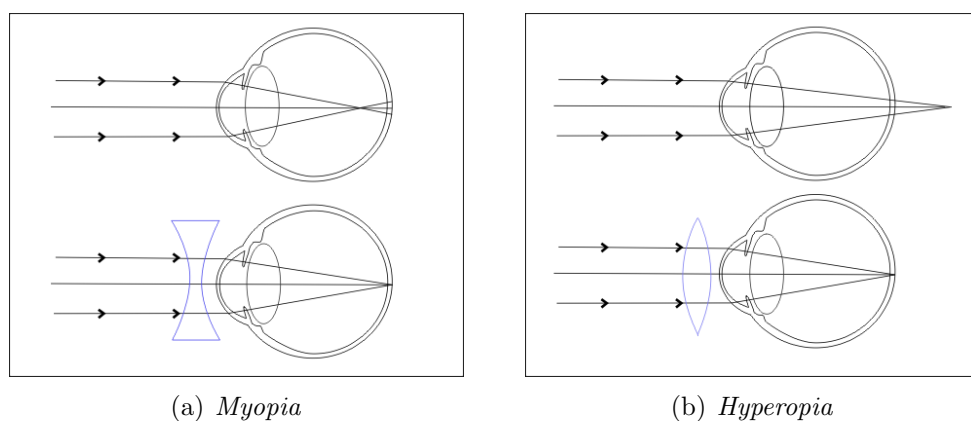


Figure 2.3: *In this figure both types of defocus and their correction methods are illustrated. Myopia [11] is corrected by a diverging or concave lens whereas Hyperopia [12] is corrected by a converging or convex lens.*

2. The Human Eye

lens is insufficient, as in hypermetropia, the image will appear blurred. Minor amounts of hyperopia are sometimes left uncorrected, however, larger amounts may be corrected with convex lenses in eyeglasses or contact lenses. One particular type of hyperopia is presbyopia which specifies the eye's diminished power of accommodation that occurs with aging. The most widely held theory is that it arises from the loss of elasticity of the crystalline lens, although changes in the lens's curvature from continual growth and loss of power of the ciliary muscles have also been postulated as its cause. Presbyopia is not a disease as such, but a condition that affects everyone at a certain age. The first symptoms are usually noticed between the ages of 40 and 50.

2.2.3 Astigmatism

Astigmatism is a refractive error of the eye in which there is a difference in degree of refraction in different meridians. It is typically characterized by an aspherical, non-figure of revolution cornea in which the corneal profile slope and refractive power in one meridian is greater than that of the perpendicular axis. For example, the image may be clearly focused on the retina in the horizontal (sagittal) plane, but not in front of the retina in the vertical (tangential) plane as it is shown in Figure 2.4. Astigmatism causes difficulties in seeing fine detail, and can often be corrected by glasses with a cylindrical lens (i.e. a lens that has different radii of curvature in different planes), contact lenses, or refractive surgery.

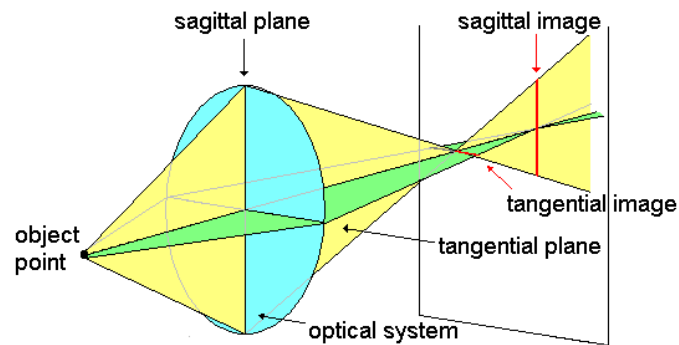


Figure 2.4: *In an astigmatic eye sagittal and horizontal image plane do not coincide. To correct astigmatism cylindrical lenses are used.*

2.2.4 Irregular Astigmatism

Any other aberration as the above mentioned, the clinician summarizes as irregular astigmatism. Usually, those aberrations cannot be corrected. One case irregular astigmatism can be corrected is the appearance of scars on the cornea. If so correction is possible with hard contact lenses as tear liquid concentrates between the cornea and the contact lens. The lower difference between the refractive indexes of the liquid and the cornea reduces the aberrations the cornea's irregular shaped surface causes.

2.3 Dynamics of the Eye

The eye is not a static system but moves incessantly [13]. This uncontrollable action makes it reasonable to not correct the eyes aberrations statically but rather dynamically or adaptive-optically [4]. Responsible for these movements are several muscles as illustrated in Figure 2.5. The medial rectus muscle moves the eye toward the nose, or adducts the eye, the lateral rectus muscle moves the eye horizontally to outer side, or abducts the eye and the superior rectus muscle elevates the eye primarily, whereas the inferior rectus

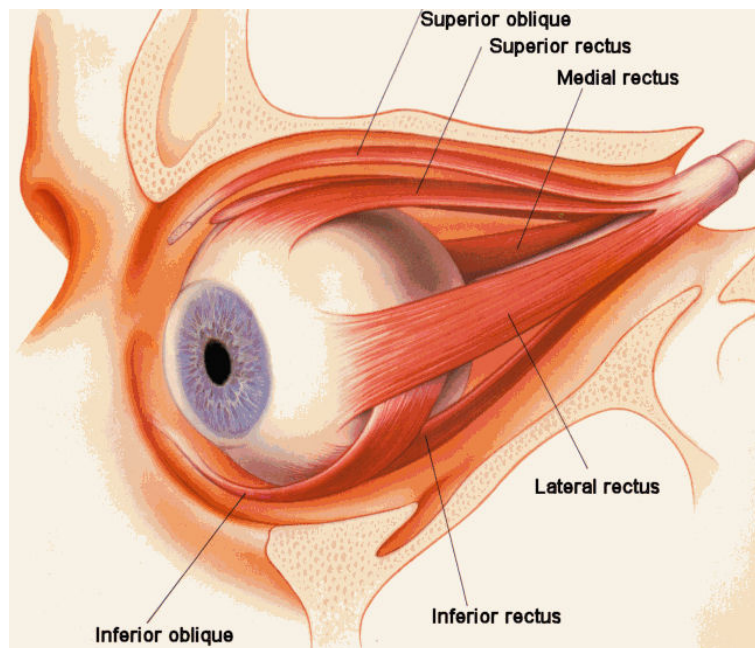


Figure 2.5: *This figure shows the six ocular muscles, that keep the eye moving incessantly [7].*

2. The Human Eye

muscle depresses the eye. The superior oblique muscle functions primarily as an intorter by rotating the vertical and horizontal axis of the eye toward the nose. The inferior oblique muscle acts to extort the eye and also serves to elevate the eye.

Humans do not look at a scene in a steady way. Instead, the eyes move around, locating interesting parts of the scene. Saccades are quick, simultaneous movements of both eyes in the same direction. The saccade is the fastest movement of an external part of the human body. The peak angular speed of the eye during a saccade reaches up to $500^\circ/\text{s}$. One reason for saccades of the human eye is that only the central part of the retina, the fovea, can image fine details. Microsaccades are a kind of fixational eye movement and typically occur during prolonged visual fixation. Microsaccades are also simultaneous movements, have amplitudes of 2-5' and last for 10-20 ms, whereas Microtremor occurs independently in both eyes, has amplitudes of 5-15" and appears with a frequency of up to 90 Hz.

2.4 Pathology

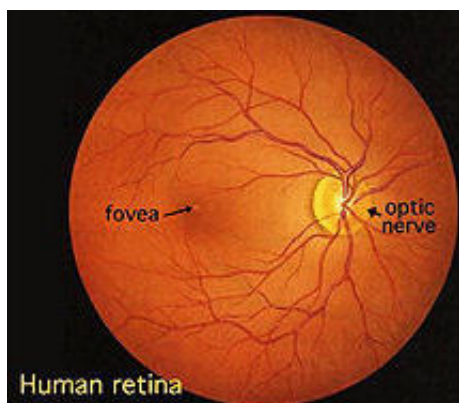


Figure 2.6: *Healthy retina as it is seen through an ophthalmoscope [7].*

without heavy pigmentation becomes easier. With wavelengths of 600 nm or above, there is a large increase in light penetration, and the choroidal vasculature becomes apparent in darkly pigmented fundi. Near-infrared imaging is well suited for investigating sub-retinal structures.

Laser Scanning Ophthalmoscopy is an important imaging technique to diagnose diseases of the eye's fundus. The color of the fundus is characterized by the mixture of reflected wavelengths determined by the amount of light reflected at various surfaces in the eye. Different retinal structures are more easily viewed at different wavelengths of light [14]. Light of short wavelengths is predominantly reflected by the retinal layers and used to view macular pigmentation and arcuate fiber bundles. As wavelength increases, seeing retinal and choroidal vessels in eyes

2.4.1 Age-related Macular Degeneration

Age-related macular degeneration (AMD) is a common retinal problem of the aging eye and a leading cause of blindness in the industrialized world [15]. Both types of AMD affect the macula, the part of the eye that allows to see fine detail. Wet AMD occurs when abnormal blood vessels behind the retina start to grow under the macula. These new blood vessels tend to be very fragile and often leak blood and fluid. The blood and fluid raise the macula from its normal place at the back of the eye. In this case damage to the macula occurs rapidly and so loss of central vision can occur quickly. Dry age-related macular degeneration occurs when the light-sensitive cells in the macula slowly break down, blurring central vision in the affected eye. As less of the macula functions, central vision is gradually lost in the affected eye. Dry AMD generally affects both eyes. One of the most common early signs is drusen. Drusen were initially described by the Dutch physiologist Donders who named them for the German word for geode, based on their glittering appearance. Drusen are tiny yellow or white accumulations of extracellular material that build up in Bruch's membrane of the eye.

Still scientists are unclear about the connection between drusen and AMD, but they do know that an increase in the size or number of drusen raises a person's risk of developing either advanced dry AMD or wet AMD. However, the presence of a few small drusen is normal with advancing age, and most people over 40 have some drusen.

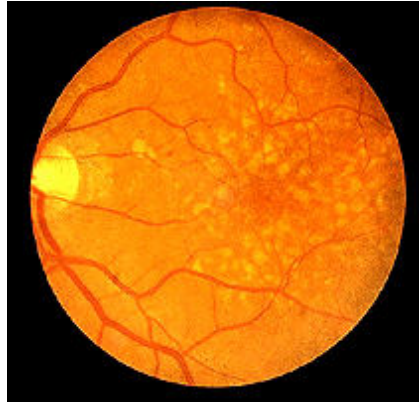


Figure 2.7: *Retina affected by AMD as it is seen through an ophthalmoscope [7].*

2.4.2 Glaucoma



Figure 2.8: *Retina affected by Glaucoma as it is seen through an ophthalmoscope [7].*

Glaucoma is not only one but a group of diseases of the optic nerve involving loss of retinal ganglion cells in a characteristic pattern of optic neuropathy [9]. Although raised intra ocular pressure is a significant risk factor for developing glaucoma, there is no set threshold that causes glaucoma. Untreated glaucoma leads to permanent damage of the optic nerve and resultant visual field loss, which can progress to blindness. A fact is, that Glaucoma is the second leading cause of blindness in the world. The two main types of glaucoma are primary open angle glaucoma (POAG), and primary angle closure glaucoma (PACG). Primary open angle

glaucoma also called chronic glaucoma is the most common type. This develops slowly so that any damage to the nerve and loss of sight is gradual. The term 'open angle' refers to the angle between the iris and sclera which is normal, in contrast to primary angle closure glaucoma where the angle is narrowed. In this condition there is a sudden increase in the pressure within one eye and the eye quickly becomes painful and red.

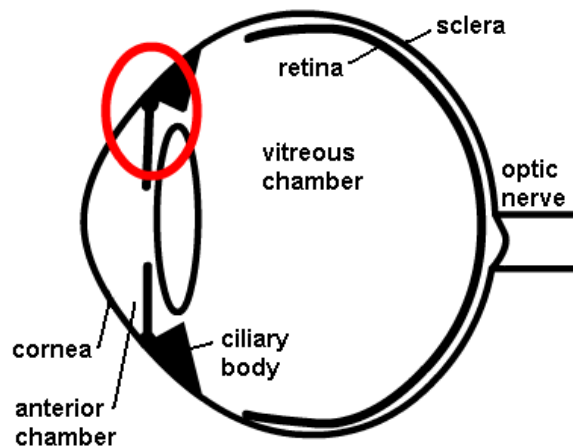


Figure 2.9: *To distinguish between different forms of Glaucoma it is important to measure the chamber angles of the patient's eyes [16].*

Chapter 3

Confocal Scanning Laser Ophthalmoscopy

Confocal scanning laser tomography is currently the most widespread non-photographic technique for imaging the optic disc and peripapillary retina in glaucoma. Although there are several available instruments, that use scanning laser tomography, almost all the published clinical and experimental work, like this one on hand as well, is based on the Heidelberg Retina Tomograph (HRT) produced by Heidelberg Engineering GmbH in Germany.

3.1 Principle of the cSLO

With the introduction of the ophthalmoscope by Hermann von Helmholtz in 1850 in vivo visualisation of the human fundus was enabled, and therefore had a major impact in the understanding of many eye conditions. In 1980, Webb's group from Boston created a device that used a laser light source to illuminate the fundus and produce an image of it on a television monitor [17]. The scanning laser ophthalmoscope (SLO), as it was termed later on, provides a high quality image of the fundus using less than 1% of the light necessary to illuminate the fundus with conventional light ophthalmoscopy. At any instant only one small area of the retina is illuminated, and the light returned from this point through the whole pupil is collected by a photomultiplier tube, which drives a TV monitor. Each pixel on the monitor corresponds directly to a pixel of the fundus. As the illuminating spot scans the fundus, the electron beam scans in synchrony the TV screen, and a picture is built up. To improve the contrast and resolution of the SLO, the confocal mode is used. In this mode, only light which is reflected from the focal plane of the

3. Confocal Scanning Laser Ophthalmoscopy

laser is detected by the photodetector. Light reflected or scattered by other retinal layers is ignored. Confocality of the system is achieved by placing a pinhole in front of the detector, which is conjugate to the laser focus.¹ The size of the pinhole determines the degree of confocality, so that a small pinhole aperture will give a highly confocal image.

¹Conjugate points are defined as any pair of points such that all rays from one point are imaged on the other within the limits of validity of Gaussian optics. This applies accordingly to conjugate planes.

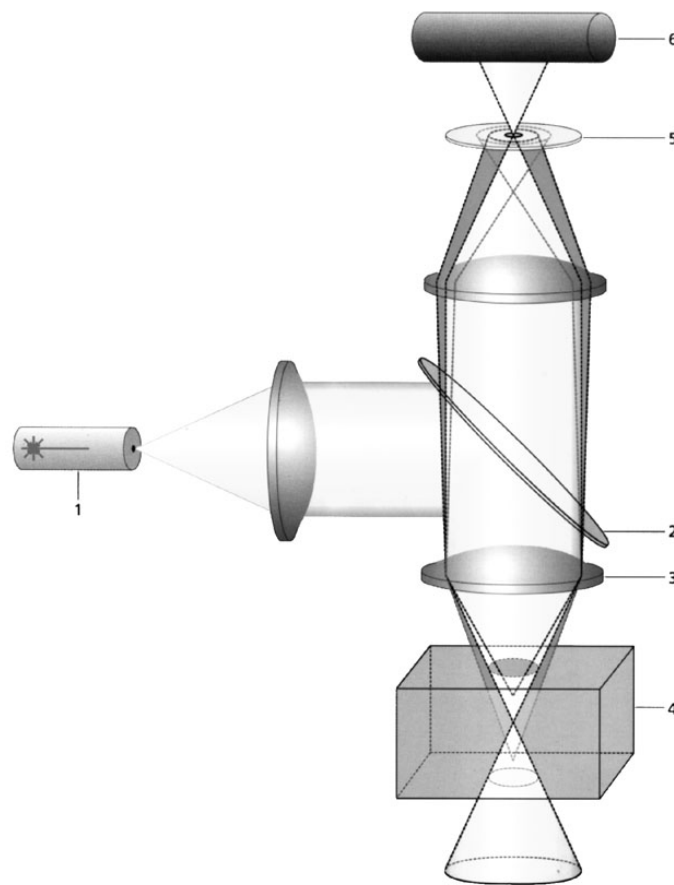
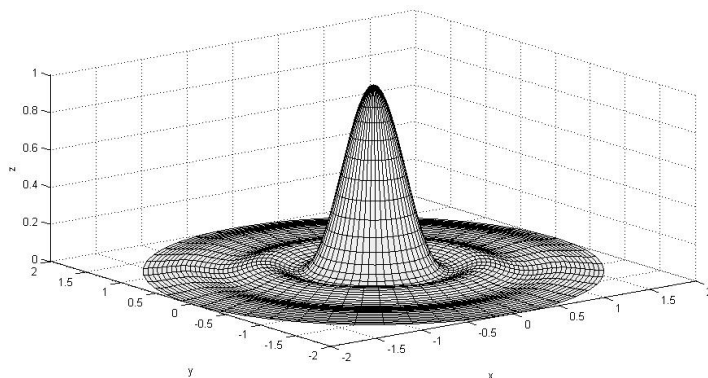


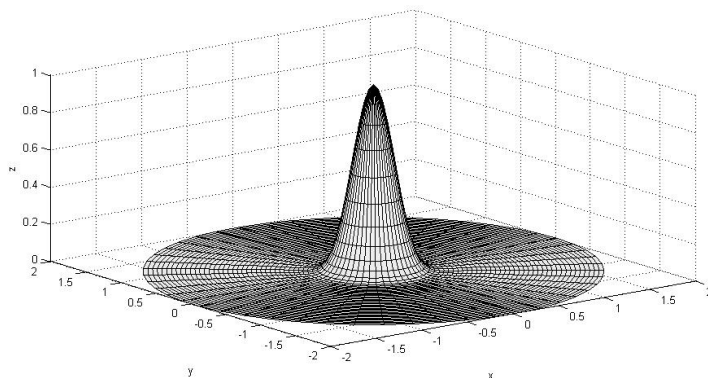
Figure 3.1: *The optical path in confocal microscopes: Light emitted by a laser source (1) illuminates via a beam splitter (2) and an objective (3) the specimen (4). Reflected light transmits the objective and the beam splitter again, passes the ocular lens and falls onto a confocal pinhole. This aperture allows light to transmit, if it arises out of the focal plane, whereas light arising out of another plane below or above the focal plane is blocked by the pinhole. A detector (6) passes the information on to a PC, which can progress the images.*

3. Confocal Scanning Laser Ophthalmoscopy

3.2 Resolution of Confocal Images



(a) $I(u) = I_0 \cdot \text{sinc}^2(\frac{u}{4})$



(b) $I(u) = I_0 \cdot \text{sinc}^4(\frac{u}{4})$

Figure 3.2: *These figures show an intensity distribution of a spot imaged by a widefield microscope (a) and by a confocal microscope (b) in comparison.*

In Figure 3.2 axial intensity distributions of a point source imaged by a widefield microscope and confocal microscope are compared [18, 19]. In widefield microscopy the distribution determined as $I(u) = I_0 \cdot \text{sinc}^2(\frac{u}{4})$ has side maxima that can be seen clearly. The variable u stands here for $u = \frac{2\pi}{\lambda} \frac{a}{f} z$ with the aperture radius a , the illuminating wavelength λ , and the focal length f . In confocal microscopy the shown distribution is described by $I(u) = I_0 \cdot \text{sinc}^4(\frac{u}{4})$. It is slimmer than the former mentioned and side maximums can hardly be recognized. This becomes important if two object points of very different intensity and small distance between each other are imaged. In the case of widefield microscopy it is possible that the darker spot

3. Confocal Scanning Laser Ophthalmoscopy

lies in a side maximum of the brighter one and therefore cannot be seen. In the case of confocal microscopy in contrast side maxima are less significant and the darker spot can be identified.

3.3 The Heidelberg Retina Tomograph

The Heidelberg Retina Tomograph (HRT) is a confocal laser scanning system for acquisition and analysis of the posterior segment of the eye [20]. This instrument consists of a camera head mounted on a slit-lamp-type stand, a control panel for operation, and a computer for control and for the display, acquisition, processing, and storage of data. The camera head contains a diode laser, emitting light at a wavelength of 670 nm, and a confocal optical system, which contains a pinhole situated in front of the detector, and a photodiode, that detects the intensity of the light reflected from the fundus.



Figure 3.3: *HRT as it is available for doctor's practices*

By scanning both horizontally and vertically in one focal plane, the instrument acquires a two-dimensional confocal image. Varying the depth of the focal plane allows acquisition of images from other planes along the z-axis (perpendicular to the optical axis). The image resolution on each plane is 256×256 picture elements (pixels), resulting in 65,536 measurements per image. An entire scan contains 32 confocal section images that are equally spaced along the z-axis, whereas the operator can vary the total scan depth and scan area, depending on the size of the optic disc and depth of the optic cup. Because of the relatively long acquisition time and the high resolution of these devices, the confocal section images must be aligned to correct for any horizontal or vertical eye movements during image acquisition. This alignment procedure ensures that each pixel location in all of the section images corresponds to the same transverse location on the fundus, allowing a graphical representation of the intensity values for that location (the intensity, or z-profile) over all image depths. Using the intensity and depth values of each pixel, the software generates a topography and reflectivity image. The primary utility of any optic disc imaging technique is to determine whether there is abnormality (detection), like glaucoma for instance, and whether there is a change (progression) in the optic disc.

Chapter 4

Adaptive Optics

In astronomy adaptive optics (AO) is used to overcome the blurring effects of atmospheric turbulence, the fundamental limitation on the resolution of ground-based telescopes. More recently, AO has found applications in other areas, most notably vision science, where it is used to correct for the eyes' wave aberration [21].

Since adaptive-optical systems are control systems, they consist of at least four items: A **control variable**, in our case the wave front, is needed, which should be corrected onto a setpoint value. A **sensor** determines the actual value of the variable to be controlled. In adaptive optics this device is known as a wave front sensor. An **actuator** is able to modulate the control variable. In case of a wave front as control variable the actuator is a phase modulator. A **control system** (including a specific control algorithm) can convert the wave aberration measurements made by the wave front sensor into a set of actuator commands that are applied to the wave front corrector.

4.1 The Wave Front and Wave Aberrations

In geometrical optics a wave front is the set of all points with same optical path length away from a particular object point. In the wave picture the wave front is a plane of constant phase which is always perpendicular to light rays.

The image-forming properties of any optical system, in particular the eye, can be described completely by the wave aberration. It is defined as the difference between the perfect (spherical) and the actual wave front for every point over the eye's pupil. A perfect eye (without aberrations) forms a perfect retinal image of point source (Airy disc). In reality, however, imperfections in the refracting ocular surfaces generate aberrations that produce a larger

4. Adaptive Optics

and, in general, asymmetric retinal image. As in this work a monochromatic light source is used only monochromatic aberrations are discussed below. The aberrations of the complete eye can be measured using a variety of different subjective and objective techniques, for instance the Shack-Hartmann wave front sensor like in this work. By using the Zernike representation (according to the Optical Society of America's Standards for reporting Optical Aberrations [22]), the wave aberration $W(r, \Theta)$ can be represented with a Zernike polynomials expansion

$$W(r, \Theta) = \sum_{n=0}^{\infty} \sum_{m=-n}^n c_n^m Z_n^m(r, \Theta) \approx \sum_{n=0}^N \sum_{m=-n}^n c_n^m Z_n^m(r, \Theta) \quad , \quad (4.1)$$

where c_n^m are scalars and Z_n^m are the Zernike polynomials, a set of functions that are orthonormal over the continuous unit circle. These functions are usually defined in polar coordinates (ρ, Θ) , where ρ is the radial coordinate ranging from 0 to 1 and Θ is the azimuthal component ranging from 0 to 2π . The conventional definition of polar coordinates $\rho = \sqrt{x^2 + y^2}$ and $\Theta = \tan^{-1}(y/x)$ is used here.

Each of the Zernike polynomials consists of three components: a normalization factor, a radial-dependent component and an azimuthal-dependent component. In this work the double indexing scheme is used for unambiguously describing these functions, with the index n describing the highest power (order) of the radial polynomial and the index m describing the azimuthal frequency of the sinusoidal component. So the Zernike polynomials are defined mathematically by

$$Z_n^m(\rho, \Theta) = \begin{cases} N_n^m R_n^{|m|}(\rho) \cos(m\Theta) & \text{for } m \geq 0, \\ -N_n^m R_n^{|m|}(\rho) \sin(m\Theta) & \text{for } m < 0 \end{cases} \quad , \quad (4.2)$$

where N_n^m is the normalization factor described in more detail below and the radial component $R_n^{|m|}(\rho)$ is given by

$$R_n^{|m|}(\rho) = \sum_{s=0}^{(n-|m|)/2} \frac{(-1)^s (n-s)!}{s! \left[\frac{n+|m|-s}{2} \right]! \left[\frac{n-|m|-s}{2} \right]!} \rho^{n-2s} \quad . \quad (4.3)$$

The normalization is given by

$$N_n^m = \sqrt{\frac{2(n+1)}{1 + \delta_{m0}}} \quad , \quad (4.4)$$

where δ_{m0} is the Kronecker delta function. The values of both n and m are always integers or zero. In addition, n can only take on positive values and

4. Adaptive Optics

Term	Zernike polynomials in spherical coordinates	Name
Z_0^0	1	Piston
Z_1^{-1}	$2\rho \sin \Theta$	Tilt in y-direction
Z_1^1	$2\rho \cos \Theta$	Tilt in x-direction
Z_2^{-2}	$\sqrt{6} \rho^2 \sin(2\Theta)$	Astigmatism $\pm 45^\circ$
Z_2^0	$\sqrt{3}(2\rho^2 - 1)$	Defocus
Z_2^2	$\sqrt{6} \rho^2 \cos(2\Theta)$	Astigmatism $0^\circ/90^\circ$
Z_3^{-3}	$\sqrt{8} \rho^3 \sin(3\Theta)$	
Z_3^{-1}	$\sqrt{8}(3\rho^3 - 2\rho) \sin \Theta$	Coma in x-direction
Z_3^1	$\sqrt{8}(3\rho^3 - 2\rho) \cos \Theta$	Coma in y-direction
Z_3^3	$\sqrt{8} \rho^3 \cos(3\Theta)$	
Z_4^{-4}	$\sqrt{10} \rho^4 \sin(4\Theta)$	
Z_4^{-2}	$\sqrt{10}(4\rho^4 - 3\rho^2) \sin(2\Theta)$	
Z_4^0	$\sqrt{5}(6\rho^4 - 6\rho^2 + 1)$	Spherical aberration
Z_4^2	$\sqrt{10}(4\rho^4 - 3\rho^2) \cos(2\Theta)$	
Z_4^4	$\sqrt{10} \rho^4 \cos(4\Theta)$	

Table 4.1: This table contains all Zernike polynomials up to 4th order (15 terms) in spherical coordinates.

for a given n , m can only take on values $-n, -n + 2, -n + 4, \dots, n$. The first 15 Zernike polynomials are listed in Table 4.1 and illustrated in Figure 4.1. Since the Zernike polynomials are orthogonal over the continuous unit circle and the lower-order terms represent familiar corneal shapes such as sphere and cylinder, the Zernike polynomials appear to be an ideal set of functions for decomposing and analyzing aberrations. Wave front sensors measure the aberrations only at a discrete number of points, and unfortunately the Zernike polynomials are not orthogonal over a discrete set of points. A technique known as GramSchmidt orthogonalization [23], however, allows the discrete set of aberration data to be expanded in terms of the Zernike polynomials and still keep the advantages of an orthogonal expansion.

4. Adaptive Optics

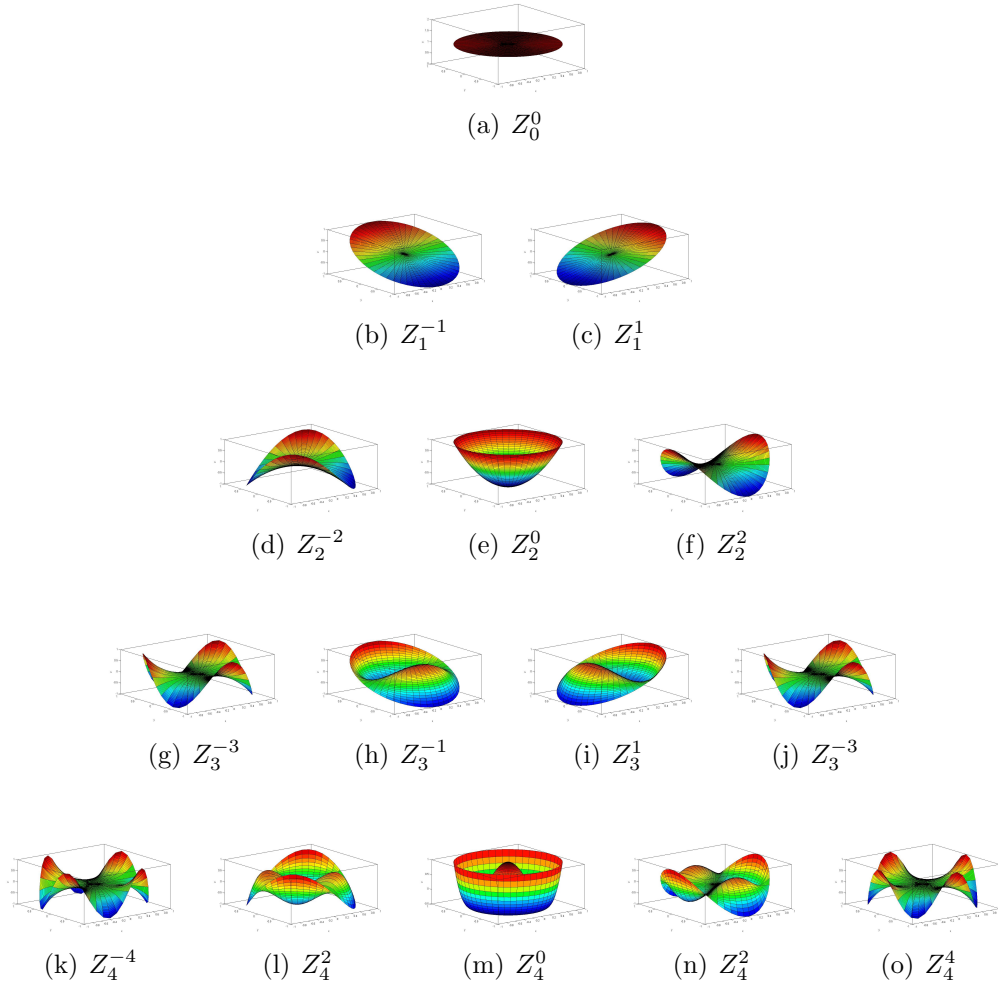


Figure 4.1: *This Figure illustrates all Zernike polynomials up to 4th order.*

4.2 Wave Front Sensors

For the eye various wave front sensing techniques have been developed. Wave front sensors measure the aberrations of the entire eye generated by both corneal surfaces and the crystalline lens and can be categorized by whether the measurement is based on a subjective or objective method and whether the wave front sensor measures the light going into the eye or coming out of the eye.

The most commonly used wave front sensors are the spatially resolved refractometer (subjective method measuring the ingoing light) [24], the laser ray tracing technique (objective method measuring the ingoing light) [25], and the Shack-Hartmann wave front sensor (objective method measuring the out-

4. Adaptive Optics

going light) [3] as it is used in this work. However, all wave front sensors developed for vision science and ophthalmology are based on the same principle, which is an indirect measurement of local wave front slopes and the reconstruction of the complete wave front by integrating these slopes.

The Shack-Hartmann wave front sensor contains a lenslet array that consists of a two-dimensional array of a few hundred lenslets, all with the same focal length ($\sim 5 \text{ mm} - 30 \text{ mm}$) and the same diameter ($\sim 100 \mu\text{m} - 600 \mu\text{m}$). The light reflected from the laser beacon projected on the retina is distorted by the wave aberration of the eye. The reflected light is then spatially sampled into many individual beams by the lenslet array and forms multiple spots in the focal plane of the lenslet. The relationship between wave front slope and the spot displacement, Δx_s and Δy_s with respect to the x and y directions, can be expressed as

$$\frac{\partial W(x, y)}{\partial x} = \frac{\Delta x_s}{F} \quad (4.5)$$

$$\frac{\partial W(x, y)}{\partial y} = \frac{\Delta y_s}{F} \quad (4.6)$$

where F is the focal length of the focusing optics. A CCD-Camera placed in the focal plane of the lenslet array records the spot array of pattern for wave front calculation. With the measured spot displacements in the x and y directions at each sampling point, the original wave front can be calculated using different reconstruction algorithms.

For a perfect eye light reflected from the retina emerges from the pupil as a collimated beam, and the Shack-Hartmann spots are formed along the op-

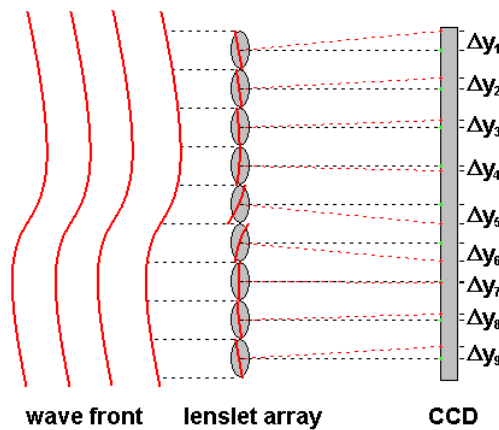


Figure 4.2: *This figure shows the principle of the Shack Hartmann Sensor. Spots of a perfect wave front are indicated green, spots of an aberrated wave front are indicated red.*

4. Adaptive Optics

tical axis of each lenslet, resulting in a regularly spaced grid of spots in the focal plane of the lenslet array. In contrast, individual spots formed by an aberrated eye, which distorts the wave front of the light passing through the eye's optics, are displaced from the optical axis of each lenslet. This displacement of each spot is proportional to the wave front slope at the location of that lenslet in the pupil and is used to reconstruct the wave aberration of the eye.

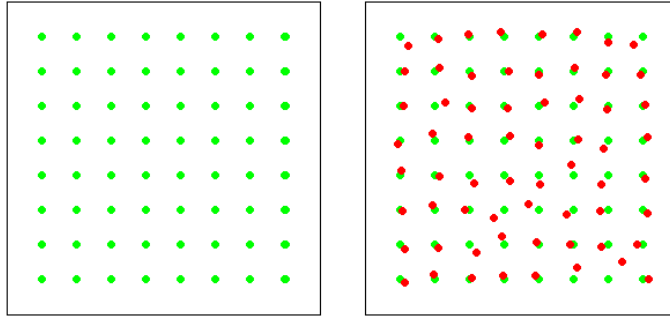


Figure 4.3: *This figure shows the Shack Hartmann spots as they are obtained by a Shack Hartmann sensor. Spots of a perfect wave front are indicated green, spots of an aberrated wave front are indicated red.*

However, the major disadvantage of the Shack-Hartmann device is its relatively small dynamic range that is limited by the lenslet spacing or number of lenslets across the pupil and the focal length of the lenslet array. The relationship between the wave front slope Θ and the spot displacement Δs can be expressed as

$$\Delta s = F \cdot \tan(\Theta) \approx F \cdot \sin(\Theta) \approx F \cdot \Theta \quad (4.7)$$

where F is the focal length of the lenslet. Larger wave front slopes will cause larger displacements of the spot.

Measurement accuracy of the wave front sensor is directly related to the precision of the centroid algorithm, that is, to the measurement precision of Δs . A conventional centroid algorithm will fail to find the correct centres of the spots if the spots partially overlap or fall outside of the virtual subaperture (located directly behind the lenslet) on the photodetector array unless a special algorithm is implemented.

The dynamic range of Θ_{max} is the wave front slope when the Shack-Hartmann spot is displaced by the maximum distance Δs_{max} within the subaperture, which is equal to one-half of the lenslet diameter for a given focal length lenslet array (when ignoring spot size). So the dynamic range can be rewrit-

4. Adaptive Optics

ten as

$$\Theta_{max} = \frac{\Delta s_{max}}{F} = \frac{d}{2F} \quad (4.8)$$

Assuming that the lenslet diameter is determined by the required number of Zernike coefficients, the only way to increase the dynamic range is to shorten the focal length of the lenslet. However, if the focal length is too short, this causes a decrease in measurement sensitivity (that is the minimum wave front slope Θ_{min} that can be measured). The measurement sensitivity can be written as

$$\Theta_{min} = \frac{\Delta s_{min}}{F} \quad (4.9)$$

where Δs_{min} is the minimum detectable spot displacement, which is normally determined by the pixel size of the photodetector, the accuracy of the centroid algorithm and the signal-to-noise ratio of the sensor. The dynamic range and the measurement sensitivity are inversely related. So increasing the dynamic range of the wave front sensor results in a decrease in its sensitivity and vice versa for a constant lenslet spacing d .

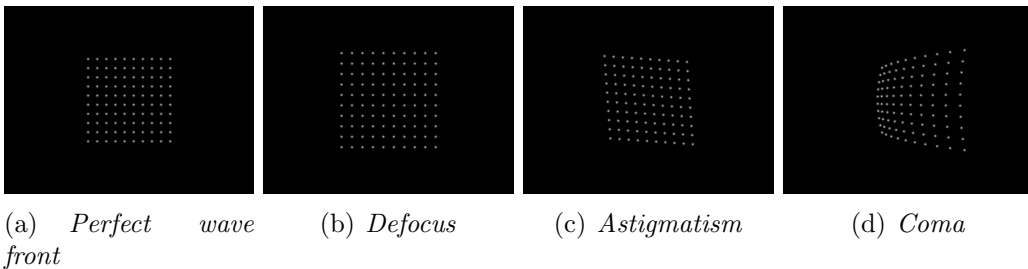


Figure 4.4: *These figures show Shack Hartmann Sensor spot pattern of wave fronts distorted by the aberrations named above. All images were generated by the simulation software of Michael Schottner [26].*

4.3 Phase Modulators

Phase modulators or wave front correctors alter the phase profile of the incident wave front by changing the physical length over which the wave front propagates or the refractive index of the medium through which the wave front passes. Most wave front correctors are based on mirror technology and impart phase changes by adjusting their surface shape. Several types of wave front correctors have been used in vision science AO systems for the correction of ocular aberrations.

4. Adaptive Optics

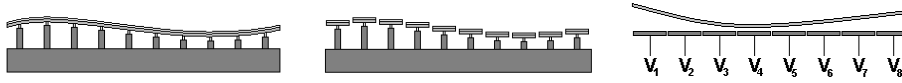


Figure 4.5: *These figures show the principle of different types of deformable mirrors as they are used in adaptive optics: A discrete actuator deformable mirror is pictured in (a), (b) shows a piston-only segmented mirror, and in (c) a membrane mirror is illustrated.*

Three types of wave front correctors are illustrated in Figure 4.5: Discrete actuator deformable mirrors consist of a continuous, reflective surface and an array of actuators, each capable of producing a local deformation in the surface. Piston-only segmented correctors consist of an array of small planar mirrors whose axial motion is independently controlled. Membrane mirrors consist of a grounded, flexible reflective membrane sandwiched between a transparent top electrode and an underlying array of patterned electrodes, each of which is capable of producing a global deformation in the surface.

4.4 The Control Algorithm

The vital link between the wave front sensor and the wave front corrector in an adaptive optics system is the control algorithm. To improve resolution the set of actuator commands that are applied to the wave front corrector should minimize the residual wave aberrations. The control algorithm's task is to convert the wave aberration measurements made by the wave front sensor into a set of actuator commands. Basically the software has to fulfill these steps:

- acquire an image of the lenslet array spots,
- find the centre of the spots and measure their displacements from a fixed reference,
- find the Zernike coefficients as a compact description of the wave front in order to completely correct aberrations that have visual significance, and
- repeat until the residual wave front error is minimized by deforming the mirror.

Regarding image acquisition it is important that the camera's frame rate is high enough. A good update target for a realtime AO loop in vision science research is 30 frames per second (fps) [21].

Once a spots image is grabbed any image processing that needs to be done is performed first. For instance, subtracting a background image, averaging

4. Adaptive Optics

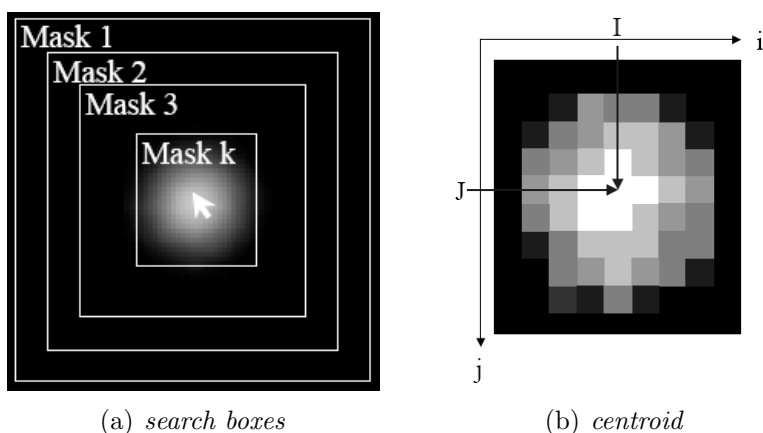


Figure 4.6: This figure illustrates the proceeding of the spot finding algorithm. It uses iterative search boxes (a), in each one searching the centre of mass (b).

frames, thresholding or flat fielding improve the likelihood of finding good spot centres.

Afterwards the software has to find the spots. One can take advantage of the fact that each spot comes from a corresponding lenslet, assuming that the optics of the system are designed so that spots lie in their lenslet's region of interest, or search box, which does not overlap the box of any other lenslet. Search boxes can be constructed initially so that they centre on a theoretical reference, a point where the spots would appear in an aberration-free system. When the set of search boxes has been determined, it is time to find each spot centre, or centroid.

The centroid algorithm normally used is an iterative one. It simply performs a standard centre-of-mass centroiding operation (which weights pixel position by intensity) but does so recursively, shrinking the box from the original size down to the size of a box that would just contain the diffraction limited spot. Each new smaller box is formed by reducing both its width and height by one pixel, and by centring it on the centroid found in the previous step.

Once all centroids are found spot displacements can be calculated. This can be done by Singular Value Decomposition, for instance, as shown below. Samples of the wave front derivative, $\partial W(x, y)/\partial x$ and $\partial W(x, y)/\partial y$, with respect to both x and y , are in the form of measured spot displacements in the wave front image, scaled by the lenslet focal length (see Equation 4.5 and Equation 4.6, respectively). When we switch to the single indexing scheme and cartesian coordinates as shown in Table 4.2 we can write Equation 4.1

4. Adaptive Optics

as

$$W(x, y) = \sum_{j=0}^{\infty} c_j Z_j(x, y) \quad . \quad (4.10)$$

Derived by x and y, respectively, this yields

$$\frac{\partial W(x, y)}{\partial x} = \sum_{j=0}^{\infty} c_j \frac{\partial Z_j(x, y)}{\partial x} \quad (4.11)$$

and

$$\frac{\partial W(x, y)}{\partial y} = \sum_{j=0}^{\infty} c_j \frac{\partial Z_j(x, y)}{\partial y} \quad . \quad (4.12)$$

Assuming we have data for K lenses, the derivatives have to be averaged over the K subapertures and Equation 4.13 and Equation 4.14 change to

$$\frac{\partial W(x_m, y_m)}{\partial x} = \sum_{j=0}^{\infty} c_j \frac{\partial Z_j(x, y)}{\partial x} \Bigg|_m \quad (4.13)$$

and

$$\frac{\partial W(x_m, y_m)}{\partial y} = \sum_{j=0}^{\infty} c_j \frac{\partial Z_j(x, y)}{\partial y} \Bigg|_m \quad . \quad (4.14)$$

Doing the approximation $J \approx \infty$ these equations can also be written as one vector equation

$$\mathbf{s}_{(2K \times 1)} = \mathbf{Z}_{(2K \times J)} \mathbf{c}_{(J \times 1)} \quad (4.15)$$

or in detail when the piston is out of interest

$$\begin{bmatrix} \frac{\Delta x_1}{F} \\ \frac{\Delta y_1}{F} \\ \frac{\Delta x_2}{F} \\ \frac{\Delta y_2}{F} \\ \vdots \\ \frac{\Delta x_K}{F} \\ \frac{\Delta y_K}{F} \end{bmatrix} = \begin{bmatrix} 1 & 0 & 2x_1 & 4x_1 & 2x_1 & \dots & \frac{\partial Z_J(x_1, y_1)}{\partial x} \\ 0 & 1 & 2y_1 & 4y_1 & -2y_1 & \dots & \frac{\partial Z_J(x_1, y_1)}{\partial y} \\ 1 & 0 & 2x_2 & 4x_2 & 2x_2 & \dots & \frac{\partial Z_J(x_2, y_2)}{\partial x} \\ 0 & 1 & 2y_2 & 4y_2 & -2y_2 & \dots & \frac{\partial Z_J(x_2, y_2)}{\partial y} \\ \vdots & \vdots & \vdots & \vdots & \vdots & \vdots & \vdots \\ 1 & 0 & 2x_K & 4x_K & 2x_K & \dots & \frac{\partial Z_J(x_K, y_K)}{\partial x} \\ 0 & 1 & 2y_K & 4y_K & -2y_K & \dots & \frac{\partial Z_J(x_K, y_K)}{\partial y} \end{bmatrix} \cdot \begin{bmatrix} c_1 \\ c_2 \\ c_3 \\ c_4 \\ c_5 \\ \vdots \\ c_J \end{bmatrix} \quad (4.16)$$

J indicates the number of Zernike coefficients that we want to recover, and 2K is twice the number of lenslets for which we have data because we have derivatives with respect to both x and y. For \mathbf{c} one can solve via

$$\mathbf{c} = \mathbf{Z}^\dagger \mathbf{s} \quad (4.17)$$

4. Adaptive Optics

Term		Zernike polynomials in cartesian coordinates	Name
Z_0^0	Z_0	1	piston
Z_1^{-1}	Z_1	x	tilt in y-direction
Z_1^1	Z_2	y	tilt in x-direction
Z_2^{-2}	Z_3	$2xy$	astigmatism $\pm 45^\circ$
Z_2^0	Z_4	$2x^2 + 2y^2 - 1$	defocus
Z_2^2	Z_5	$y^2 - x^2$	astigmatism $0^\circ/90^\circ$
Z_3^{-3}	Z_6	$3xy^2 - x^3$	
Z_3^{-1}	Z_7	$3x^3 + 3xy^2 - 2x$	coma in x-direction
Z_3^1	Z_8	$3y^3 + 3x^2y - 2y$	coma in y-direction
Z_3^3	Z_9	$y^3 - 3x^2y$	
Z_4^{-4}	Z_{10}	$4xy^3 - 4x^3y$	
Z_4^{-2}	Z_{11}	$8x^3y + 8xy^3 - 6xy$	
Z_4^0	Z_{12}	$6x^4 + 6y^4 + 12x^2y^2 - 6x^2 - 6y^2 + 1$	spherical aberration
Z_4^2	Z_{13}	$4y^4 - 4x^4 + 3x^2 - 3y^2$	
Z_4^4	Z_{14}	$y^4 - 6x^2y^2 + x^4$	

Table 4.2: Zernike polynomials up to 4th order (15 terms)

In the above notation, the elements, z' , of the matrix \mathbf{Z} are the derivatives of the basis functions, Z , and the dagger indicates pseudo-inverse. The coefficients of \mathbf{c} result from multiplying the pseudo-inverse of the derivative of the Zernike polynomials, \mathbf{Z}^\dagger , by the slope vector, \mathbf{s}

$$\begin{bmatrix} c_1 \\ c_2 \\ c_3 \\ \vdots \\ c_J \end{bmatrix} = \begin{bmatrix} z'_{11} & z'_{12} & z'_{13} & z'_{14} & \cdots & z'_{1(2K-1)} & z'_{1(2K)} \\ z'_{21} & z'_{22} & z'_{23} & z'_{24} & \cdots & z'_{2(2K-1)} & z'_{2(2K)} \\ z'_{31} & z'_{32} & z'_{33} & z'_{34} & \cdots & z'_{3(2K-1)} & z'_{3(2K)} \\ \vdots & \vdots & \vdots & \vdots & \vdots & \vdots & \vdots \\ z'_{J1} & z'_{J2} & z'_{J3} & z'_{J4} & \cdots & z'_{J(2K-1)} & z'_{J(2K)} \end{bmatrix} \cdot \begin{bmatrix} \frac{\Delta x_1}{F} \\ \frac{\Delta y_1}{F} \\ \frac{\Delta x_2}{F} \\ \frac{\Delta y_2}{F} \\ \vdots \\ \frac{\Delta x_K}{F} \\ \frac{\Delta y_K}{F} \end{bmatrix} \quad (4.18)$$

Chapter 5

Setup

5.1 Hardware

For this work a conventional Heidelberg Retina Tomograph as it is described in section 3.3 was modified. The optical path of the whole aperture is schematically shown in Figure 5.1 and a photo of the original setup is shown in Figure 5.3.

The illuminating laser beam is injected into the model eye via the HRT. Thereby it is necessary to set up a telescope to image the scan pupil onto the pupil of the model eye. This telescope also serves as defocus correction so that it is even possible to get a rather sharp image of an aberrated eye's fundus. The laser beam then is focused onto the surface of the model eye retina by the model eye lens. The light scattered back from the point source on the retina exits the eye through the pupil.

The beamsplitter cube B1 is designed to provide a 50:50 split ratio and to work over a broad wavelength range from 700 nm to 1100 nm. The entrance and exit faces are antireflection coated while the diagonal internal surface has the broadband beam splitting coating. It divides the outgoing beam into one leading to the Shack-Hartmann sensor and another one leading to the diode of the HRT. This diode is connected to a personal computer that runs the conventional HRT software, which is called the Heidelberg Eye Explorer. The telescope consisting of lens L1 and L2 serves to telecentrically image the pupil plane (and the scan pupil, respectively) onto the lens array. Here a ratio of 2:1 was used to halve the beam diameter so that all the Shack-Hartmann spots of the microlenses, that are illuminated by the laser source, fit onto the CCD camera. The wave front in the plane of the SHS lenslet array is sampled by the central part of the lenslet array and focused directly onto the CCD camera to form the 2-D focal spot image. This CCD camera is

5. Setup

connected to another personal computer, which is used for grabbing, storing and preprocessing the Shack Hartmann images. The frame grabber in this PC is able to grab 30 pictures per second.

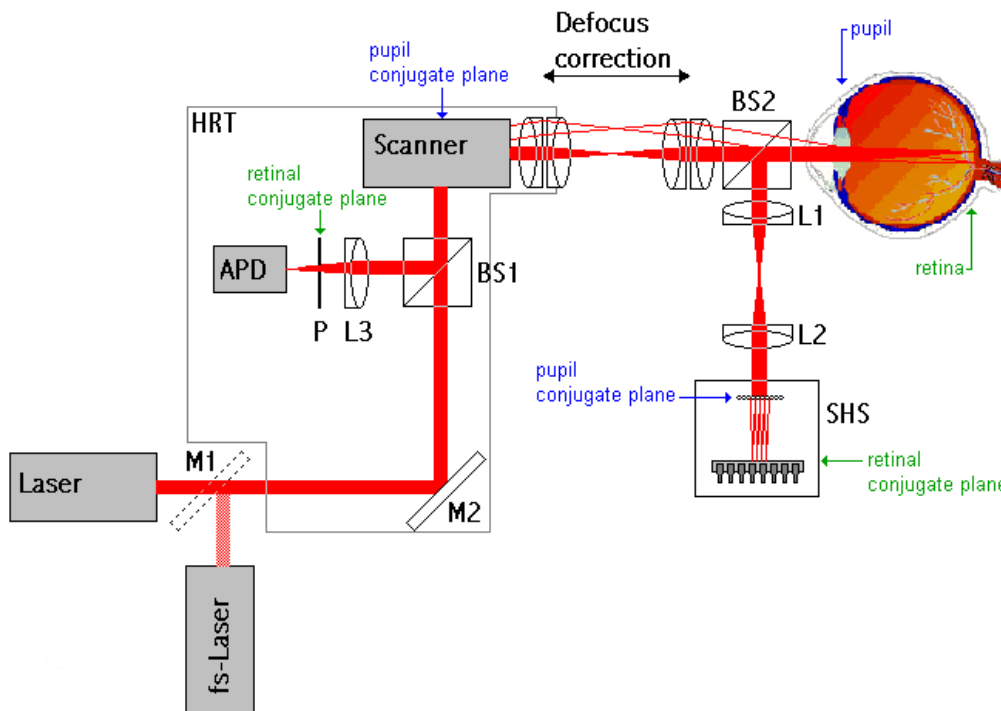


Figure 5.1: *This is a drawing of the optical path in the setup. Conjugate pupils are here the lens of the model eye, the scan pupil, and the lenslet array of the Shack Hartmann Sensor.*

The Laser Diode The original illumination source of the HRT was replaced by a wavelength division multiplexer (ozoptics) with an output wavelength of 830 nm. This wavelength was chosen because of mainly two reasons. The first reason is that several studies proved near infrared light providing better visibility than visible light for sub-retinal features [14, 27]. Contrast and visibility of features increases with increasing wavelength, at least in the range from 795 to 895 nm. The second reason is that in living eyes it is possible to illuminate the retina for a longer period with light of longer wavelengths without causing damage to the retina cells than with light of shorter wavelengths.¹ The laser power was tunable and a maximal power of 3.25 mW could be reached.

¹This fact results from the power equation $P = \frac{h \cdot c}{t \cdot \lambda}$.

5. Setup

The femtosecond Laser In addition to the diode laser source a Nd:Glass laser of 1054nm wavelength could be injected into the optical path. To switch between the two light sources easily, a fold-away beamsplitter was implemented into the optical path. If it was situated into the course of beam, it blocked the laser diode beam whereas it reflected the femtosecond laser beam into the HRT. The femtosecond laser was not used for wavefront measuring purpose.

The Scanner The scanning system of the HRT consists of a galvanometer scanner for the slow (horizontal) and a resonant scanner for the fast (vertical) scan direction. Recording one image lasts 32 ms but due to a dead time of the photo diode in the HRT of 16 ms image acquisition frequency shrinks to 20,83 images per second. By automatically shifting the confocal pinhole also a depth scan is made. Recording a whole z-scan of 32 single images is possible in 1.54 s. In our setup x-y-scan angles could be chosen between 1° , 5° and 10° . With these scan angles it was also possible to take ophthalmoscope images as shown in Figure 5.2. Furthermore, the scanner could operate in the freeze modus, so the scanner was only scanning over 0.5° and the scanner could be switched off completely. Using these modi no ophthalmoscope images could be gained.

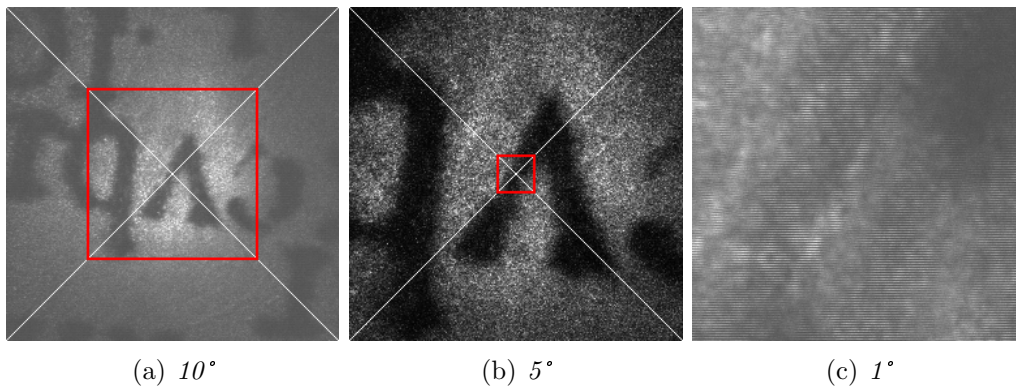


Figure 5.2: *Ophthalmoscope images with different scan angles.*

The Model Eye As model eyes a human model eye and a rat model eye, respectively, were used. A model eye consists of a lens and a piece of printed paper located in the focal plane of the lens. In case of the human model eye a lens with a focal length of 17 mm and a diameter of 8 mm was used. The lens diameter corresponds to the achievable dilated pupil size of a real

5. Setup

human eye. In case of the rat model eye a lens with a focal length of 9 mm and a diameter 5 mm was used.

The Sensor The Shack-Hartmann-Sensor was realized by placing a lenslet array of Adaptive Optics Associates in front of a cooled CCD-Camera of SAC-imaging (SAC9). The CCD image resolution is 640×480 pixels with each pixel size of $8.6 \mu\text{m} \times 8.6 \mu\text{m}$ and a 10 bit dynamic range. This corresponds to 1024 grey scales. With the SAC9 camera it was possible to grab 30 frames per second in full resolution. The microlenses of the chosen lenslet array have a distance of $400 \mu\text{m}$ between each other (also called pitch) and a focal length of 53 mm. Each lenslet of the Shack Hartmann Sensor covers an area of 46.5×46.5 pixels in the CCD plane. Because the telescope between model eye and sensor caused a demagnification of 2, the beam diameter was halved and therefore the slope was doubled. These considerations are paid attention to in the evaluation software.

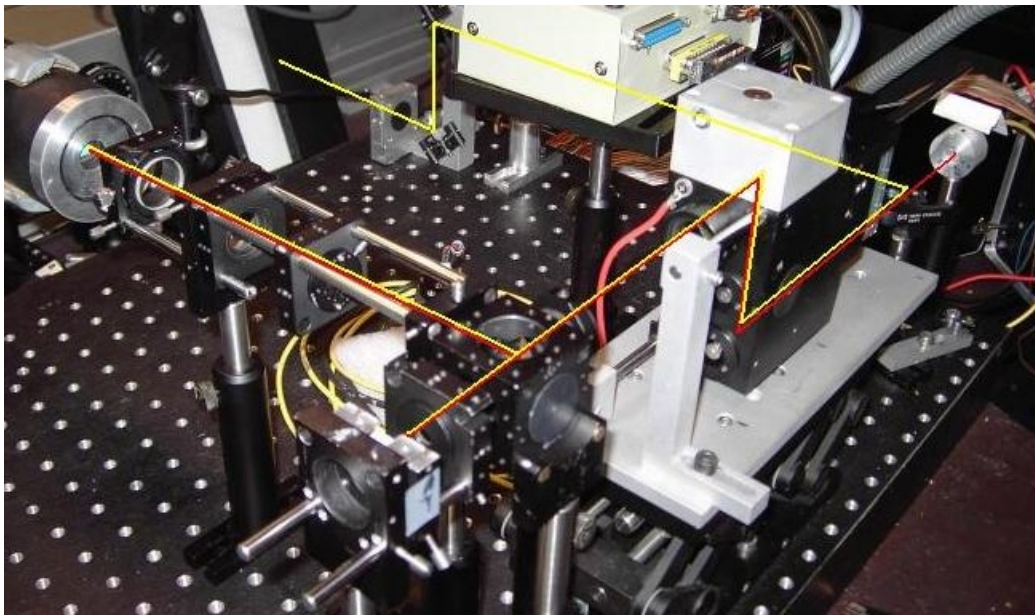


Figure 5.3: *This figure shows the original setup with illustrated light path of the fs-laser (yellow) and the laser diode (red).*

5.2 Software

To grab and store images I used the software that belongs with the camera SAC9. As this camera is in general used for astronomical imaging, it is called AstroVideo.

To preprocess the images I used the free ImageJ software available on <http://rsb.info.nih.gov/ij/>. For improving image quality, all images were averaged and afterwards the also averaged background was subtracted. Finally, I enhanced contrast so that 0.01% of all pixels were saturated. As it is proved in Figure 5.4 a saturation of 0.01% of the pixel still ensures a reliable spot finding algorithm. The surface plot of gray values shows the 9 brightest spots lying in the central area of the Shack-Hartmann spots image.

Preprocessed images were stored as bitmap-files (*.bmp) and then evaluated by the software HSS written by Michael Schottner and explained in detail in his dissertation [26]. The software calculates the Zernike coefficients out of spot displacements, while all necessary parameter like sublens diameter, pixel size of the ccd camera and magnifying telescopes, for example, are considered.

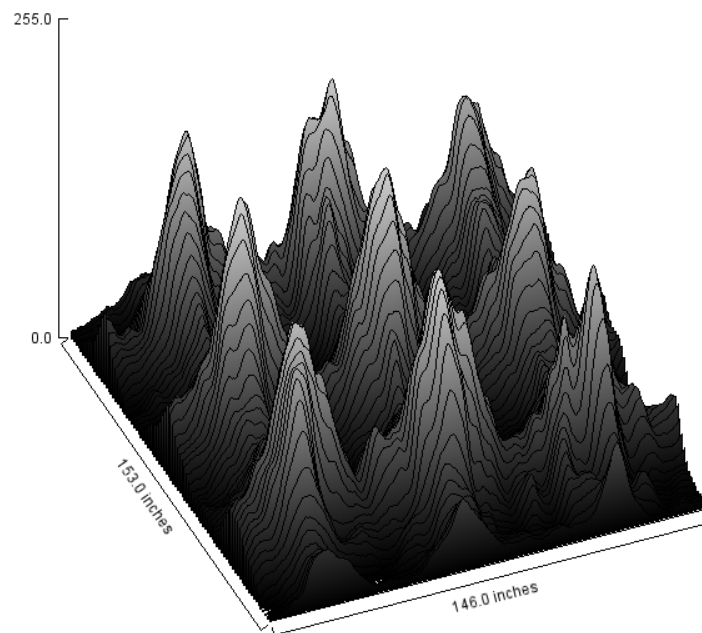


Figure 5.4: *These plots shows a surface plot of gray values. As this curve is smooth a saturation of 0.01% of the pixels enhances the reliability of the centroiding algorithm.*

Chapter 6

Results

6.1 Measurement and Evaluation

To test this wave front sensing Scanning Laser Ophthalmoscope with living eyes it is important that the laser power is not too high. Therefore the power of the laser diode at the model eye's pupil was always kept at $6\ \mu\text{W}$ or less for wave front measurements or fundus imaging. This is more than 100 times smaller than the maximum permissible exposure for continuous viewing at this wavelength [28].

To take Shack Hartmann spot images, there were basically two ways to do this: As the scanner was very fast and only needed 32 ms for one whole single scan and the framegrabber's limit was to grab one image in 33 ms, spots became too blurred when taking spot images during a scan with a big scan angle. So the first possibility was to switch the scanner to the freeze-mode where it was only scanning over an angle of $0.5 \times 0.5^\circ$.

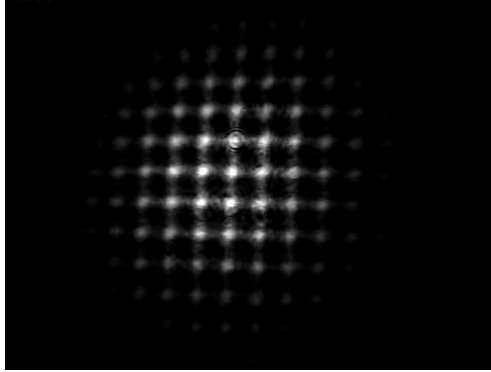
The second possibility was to switch off the scanner completely. Although this step usually results in bad quality images as speckles¹ appear in the image, this turned out to be the better way. The laser diode I used has a short coherence length resulting in less speckles in the Shack Hartmann spots than when using a coherent laser source. Still one can see speckles in the images, but the software was able to reliably gain the Zernike coefficients.

Some taken images on a human model eye are shown below. Figure 6.1 (a) shows the Shack-Hartmann spot pattern of an unaberrated model eye. Spots are still not perfectly equidistant because of system aberrations. This image is used as reference image. Figure 6.1 (b) shows the Shack-Hartmann spot

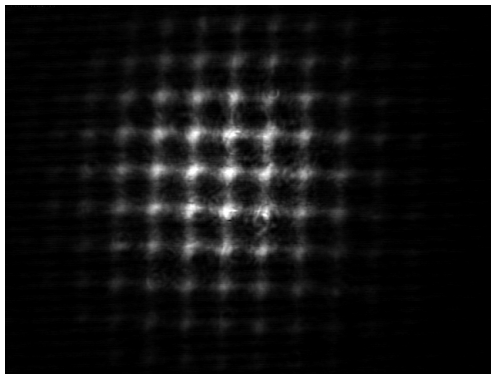
¹Speckles are spatially random intensity distributions produced from the coherent interference of light that reflects from an optically rough surface or propagates through a turbulent medium.

6. Results

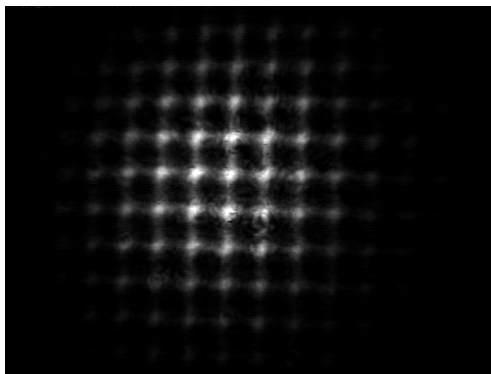
pattern of a model eye aberrated by an astigmatic lens and Figure 6.1 (c) a model eye aberrated by a defocal lens.



(a) unaberrated model eye



(b) astigmatic model eye



(c) defocal model eye

Figure 6.1: *Shack Hartmann spots of a model eye without aberration (a) and aberrated by astigmatism (b) and defocus (c), respectively.*

6. Results

Table 6.1 contains the first 4 orders of Zernike coefficients without units, that is, not standardized onto the pupil. As the piston Z_0 cannot be calculated it is not considered here. Having gained Zernike coefficients, the best correction by astigmatic and confocal lenses can also be calculated by the software. In case of the spot images shown in Figure 6.1, we get for the astigmatic model eye a defocus of -0.19587 DS and an astigmatism of -2.4066 DC with an axis of 165.975° . For the defocal eye a defocus of -0.41254 DS and an astigmatism of -0.7545 DC with an axis of 171.283° was calculated. This seems to be reasonable as I used an astigmatic lens of -2.5 DC and a defocal lens of -0.5 DS for the test measurements presented here. In Table 6.1 and Figure 6.1 the 14 Zernike coefficients are illustrated in diagrams.

Term	Zernike polynomials of an astigmatic lens	Zernike polynomials of a defocal lens	Name
Z_1	-0.000894463	0.001782818	Tilt in y
Z_2	-0.000441715	0.000346664	Tilt in x
Z_3	0.000369128	0.001848045	Astigmatism $\pm 45^\circ$
Z_4	0.001823945	0.003231278	Defocus
Z_5	-0.001175501	-0.003468369	Astigmatism $0^\circ/90^\circ$
Z_6	-0.000249881	-0.001183771	
Z_7	-0.000155659	-0.000198111	Coma in x
Z_8	-0.000151466	-0.000569209	Coma in y
Z_9	0.000305387	0.000621058	
Z_{10}	-0.000057627	-0.000362092	
Z_{11}	0.000126923	0.000333755	
Z_{12}	0.000000033	0.000401334	Spherical aberration
Z_{13}	0.000052089	-0.000846666	
Z_{14}	0.000039092	0.001576040	

Table 6.1: This table contains all Zernike polynomials gained by the spot images shown above up to 4^{th} order in spherical coordinates. Tilt is not considered in the evaluation.

6. Results

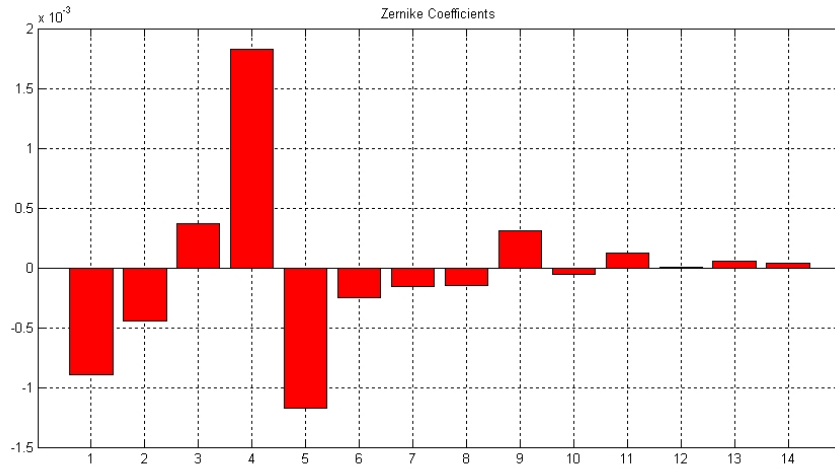


Figure 6.2: In this figure the Zernike coefficients calculated out of the spot pattern shown in Figure 6.1 (b) are illustrated. For this measurement the model eye was aberrated by an astigmatic lens of -2.5 DC.

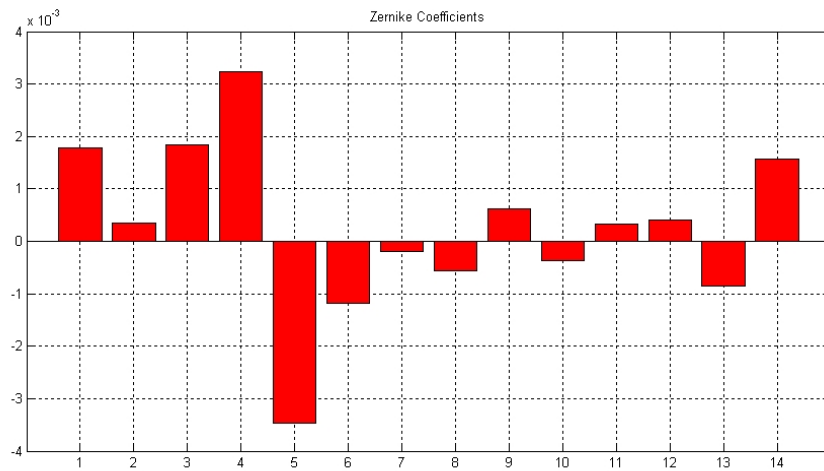


Figure 6.3: Here the Zernike coefficients calculated out of the spot pattern shown in Figure 6.1 (c) are illustrated. For this measurement the model eye was aberrated by a defocal lens of -0.5 DC.

6.2 Discussion and Future Prospect

In this work a wave front sensing confocal Scanning Laser Ophthalmoscope was built and tested. The confocal Scanning Laser Ophthalmoscope that was modified for this purpose is known as a Heidelberg Retina Tomograph built by Heidelberg Engineering. As this Ophthalmoscope is compact, manipulations were limited. By measuring the wave front in between scanner and model eye, I was forced to stop the scanner while taking a spot image. By a trigger this stopping procedure could be as short as 50 ms. Considering that the operating power of the laser was kept far under the permitted power this would not be of any harm to the patient, but keeping in mind to build a real-time closed loop adaptive-optical system this is very unhandy. Besides stopping and starting the scanner over and over will show signs of wear by the time. Although the wave front sensor was working properly, this setup should be modified in future. One setup improving the setup presented in this work will be built at the Ruprecht-Karls-Universität in Heidelberg and is explained below.

AO-cSLO

For setting up a new adaptive-optical confocal Scanning Laser Ophthalmoscope the layout shown in 6.2 was chosen. The AO-cSLO occupies approximately a $1.5\text{ m} \times 1\text{ m}$ area on an optical table. Here the light beam of a laser diode is measuring about 3mm in diameter. To use the deformable mirror (DM) ideally, this beam is expanded by a 1:3 telescope. The 9 mm laser beam then passes a polarizing beam splitter (PBS) and, thus, is linearly polarized. Afterwards it is reflected by a mirror (M) onto the deformable mirror and demagnified again by a 3:1 telescope. The scanner is still the conventional one of the HRT. It scans the beam over the pupil of the model eye. The telescope between scanner and eye functions as a relay telescope without any magnification. In front of the eye a $\lambda/4$ -retarder causes light entering the eye to be circularly polarized. The lens of the model eye focusses the beam onto a point on the retina. Due to the varying directions out of which light enters the eye, also the retina is scanned. Light reflected by the retina exits the eye again, is caused to be linearly polarized (but perpendicular to the incoming light) by the wave-retarder and descanned by the scanner. Because velocity of light is much higher than the velocity of the scanner this consideration is justified. After the scanner the beam is expanded again and reflected by the deformable mirror and the mirror. Because polarization is rotated by 90° , light is now reflected by the polarizing beamsplitter. In this arm the ophthalmoscope image is gained by the photodiode (APD) and the spot image

6. Results

by the Shack-Hartmann sensor (SHS). Aberrations measured by the SHS are corrected by the deformable mirror in a closed loop circuit.

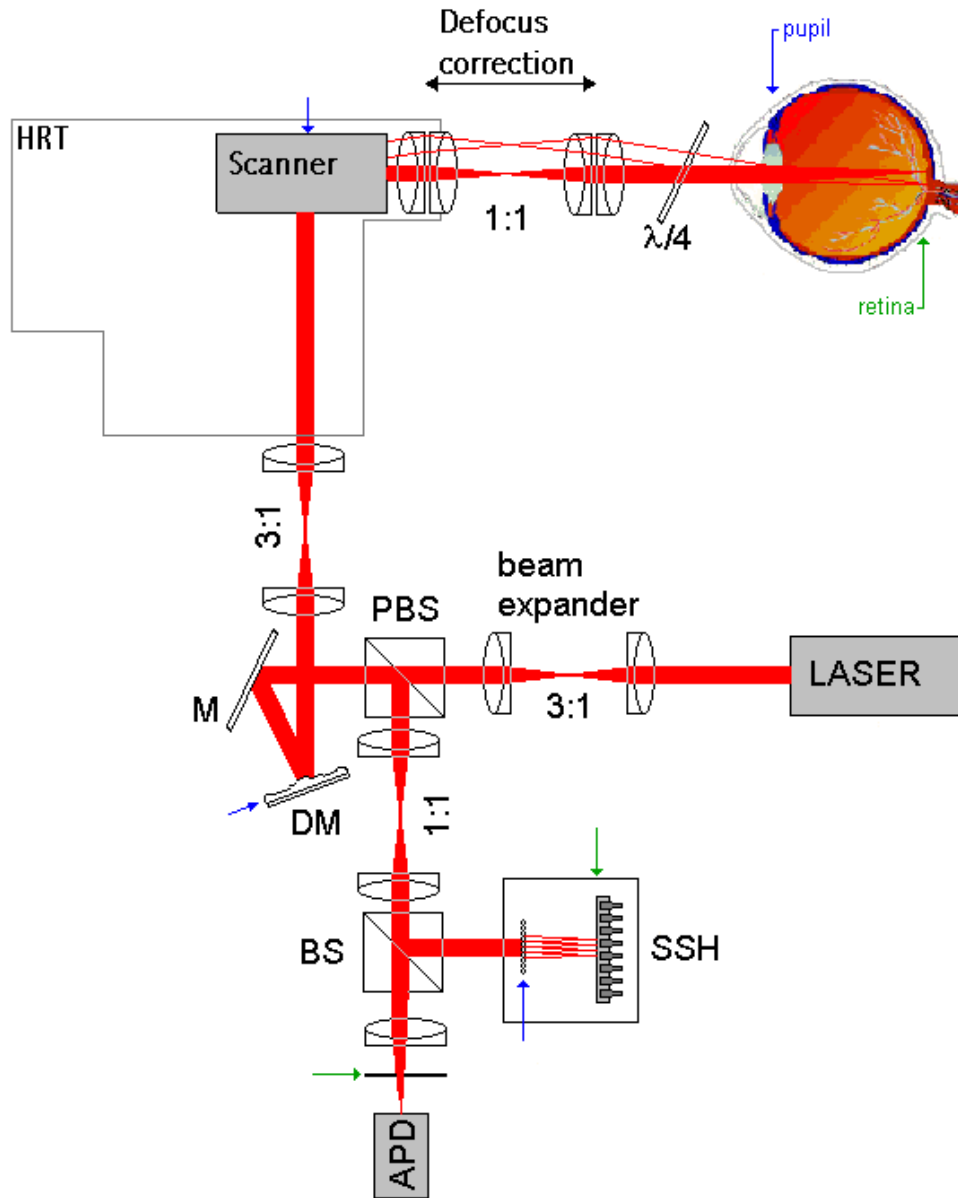


Figure 6.4: This outline shows an AO-cSLO as it will be set up in Heidelberg. Because of the scanning and descanning principle as it is explained in the text image quality of the Shack-Hartmann spot images is expected to be much higher.

Bibliography

- [1] Babcock, H. W. The Possibility of Compensating Astronomical Seeing. *Publication of the Astronomical Society of the Pacific* (1953). 1
- [2] Max, C. *et al.* The core of NGC 6240 from Keck adaptive optics and Hubble Space Telescope NICMOS observations. *The Astrophysical Journal* (2005). 1
- [3] Liang, J. *et al.* Objective measurement of wave aberrations of the human eye with the use of a Hartmann-Shack wave-front sensor. *Journal of the Optical Society of America A* (1994). 2, 20
- [4] Hofer, H. *et al.* Dynamics of the eye's wave aberration. *Journal of the Optical Society of America A* (2001). 2, 8
- [5] Dreher, A. W. *et al.* Active optical depth resolution improvement of the laser tomographic scanner. *Applied Optics* (1989). 2
- [6] Sheinman, J. www.sheinman.com/Aanatomyintro.htm. 3
- [7] Kolb, H. *et al.* www.webvision.med.utah.edu. 3, 4, 5, 8, 9, 10, 11
- [8] Bille, J. & Schlegel, W. *Medizinische Physik Band 3* (Springer Verlag, Berlin, Heidelberg [u.a.], 2005). 3
- [9] Morrison, J. C. & Pollack, I. P. *Glaucoma - Science and Practice* (Thieme Medical Publishers, Inc, New York, Stuttgart, 2003). 3, 11
- [10] Artal, P. *et al.* Compensation of corneal aberrations by the internal optics in the human eye. *Journal of Vision* (2001). 6
- [11] <http://en.wikipedia.org/wiki/Hyperopia>. 6
- [12] <http://en.wikipedia.org/wiki/Myopia>. 6
- [13] Schmidt, R. F. & Thews, G. *Physiologie des Menschen* (Springer, 1997). 8
- [14] Elsner, A. E., Burns, S. A., Weiter, J. J. & Delori, F. C. Infrared Imaging of Sub-retinal Structures in the Human Ocular Fundus. *Vision Research* (1995). 9, 28
- [15] Holz, F. G., Pauleikhoff, D., Spaide, R. F. & Bird, A. C. *Age-related macular degeneration* (Springer-Verlag, 2004). 10
- [16] www.goodhope.org.uk/departments/eyedep/glaucoma.htm. 11
- [17] Webb, R. *et al.* Flying spot TV ophthalmoscope. *Applied optics* (1980). 12
- [18] Pérez, J.-P. *Optik* (Spektrum Akademischer Verlag, 1996). 14

Bibliography

- [19] Sommerfeld, A. *Optik* (Akademische Verlagsgesellschaft Geest & Portig K.-G., 1964). 14
- [20] Heidelberg Engineering GmbH, G., Heidelberg. *The Heidelberg Retina Tomograph II* (2003). 15
- [21] Porter, J., Queener, H., Lin, J., Thorn, K. & Awwal, A. *Adaptive Optics for Vision Science* (Wiley-Interscience, 2006). 16, 23
- [22] Thibos, L., Applegate, R. & Schwiegerling, J. Standards for Reporting the optical Aberrations of Eyes. *Trends in Optics and Photonics, Vision Science and Its Applications* (2000). 17
- [23] Wang, J. & Silva, D. Wave-front interpretation with Zernike polynomials. *Applied Optics* (1980). 18
- [24] Webb, R. *et al.* Measurement of Ocular Local wavefront Distortion with a Spatially Resolved Refractometer. *Applied Optics* (1992). 19
- [25] Navarro, R. *et al.* Monochromatic aberrations and point-spread functions of the human eye across the visual field. *Journal of the Optical Society of America A* (1998). 19
- [26] Schottner, M. *Algorithms for the application of Hartmann-Shack wavefront sensors in ophthalmology*. Ph.D. thesis, Universität Heidelberg (2002). 22, 31
- [27] Berendschot, T. T. *et al.* Fundus reflectance — historical and present ideas. *Progress in Retinal and eye Research* (2003). 28
- [28] ANSI. *American National Standard for the Safe Use of Lasers Specifications (ANSI Z136.1, 2000*. FL: Laser Institute of America (2000). 32

Acknowledgments

Here I would like to express my gratitude to all those people who helped me in completing this Master Thesis.

In particular thanks to

- **Prof. Dr. Frederick Fitzke**
for giving me the opportunity to work on this interesting topic and for his support and professional scientific advice during my time in his group in the Department for Visual Science.
- **Prof. Dr. Josef Bille**
for offering me to take part in this Master Program.
- **Vy Luong**
for his appreciated advice in and around the world of computers and electronics and his helpfulness to organize all the equipment needed.
- **Dr. Nina Korablinova**
for her advice and for helping me with the image evaluation.
- **Olivier La Schiazza and Mikael Agopov**
for their support and advice via telephone and email.
- **Felix Frank**
for sharing numberless hours in and out the lab.
- **My family**
for their encouragement and support throughout my years of study.

Furthermore, I would like to thank the "Landesstiftung Baden-Württemberg" for financially supporting my stay in London.